Optimization of second-harmonic generation from touching plasmonic wires

Shimon Elkabetz [ORCID],[1,*] K. Nireekshan Reddy [ORCID],[1,†] Parry Y. Chen,[1] Antonio I. Fernández-Domínguez,[2] and Yonatan Sivan [ORCID][1]

[1]*School of Electrical and Computer Engineering, Ben-Gurion University of the Negev, Beer-Sheva 8410501, Israel*
[2]*Departamento de Física Teórica de la Materia Condensada and Condensed Matter Physics Center (IFIMAC),*
Universidad Autónoma de Madrid, E-28049 Madrid, Spain

We employ transformation optics to optimize the generic nonlinear wave interaction of second-harmonic generation (SHG) from a pair of touching metallic wires. We demonstrate a six orders of magnitude increase in efficiency with respect to SHG from a single wire, and a ten orders of magnitude increase in the second-harmonic scattered power by increasing the background permittivity. These results have clear implications for the design of nanostructured metallic frequency-conversion devices. Finally, we exploit our analytic solution of a nontrivial nanophotonic geometry as a platform for performing a critical comparison of the strengths, weaknesses, and validity of other prevailing theoretical approaches previously employed for nonlinear wave interactions at the nanoscale.

I. INTRODUCTION

The advent of lasers has opened the gateway to studying various nonlinear optical effects and to harnessing them for practical purposes. The simplest of these effects are the second-order nonlinear processes, and in particular, their degenerate version, second-harmonic generation (SHG). Using standard nonlinear optical materials, commercial devices based on SHG are already available (e.g., a green laser pointer). Nevertheless, recent advances in fabrication technology may pave the way towards further increases of device efficiency via nanostructuring. Of particular interest in this context are metal-dielectric nanostructures that benefit from the large field intensities associated with plasmonic resonances [1].

Theoretical research into this problem has focused on two somewhat distinct aspects. First, attention has been devoted to understanding the correct description of the underlying optical response of the metal itself, starting from standard electroniclike second-order polarization tensors or even simpler surface polarization tensors [2] all the way to hydrodynamic models with growing complexity (see [3,4]). The latter set of studies included the identification of the relative importance of the various terms in the model [5–8] and its specialization to even more complex spatial configurations such as few-nanometer heterodimers [9,10]. Second, efforts have been dedicated to understanding the wave physics associated with second-harmonic (SH) generation from various structures of interest (see, e.g., [11–16]), connecting it to the linear response using simple models [11,17–19], understanding the underlying symmetries [20–22], optimizing the response (see, e.g., [23,24]), and designing applicable devices [25]. Similarly

to the linear response of complex metallic nanostructures, fully analytical solutions are available for only a limited number of simple geometries. Accordingly, previous theoretical work mostly involved numerical simulations, and usually addressed only the far-field properties of the SH fields [15].

In [26], we introduced an analytic tool for this class of problems, namely, transformation optics (TO). This technique rose to fame in facilitating the design of the invisibility cloaks [27], and was later used for the interpretation and design of a range of plasmonic structures [28–31]. Our implementation uses TO to study nonlinear optical wave mixing. Specifically, we analytically calculated the SH field generated by a pair of identical touching metal wires (TWs); for convenience of the reader, the complete details of this calculation are provided in Appendix A.

The transformation optics approach enabled several *qualitative* insights. First, it provided a simple interpretation of the analytic solution (A1): The fundamental frequency (FF) plane wave which is incident upon the TWs [see Fig. 1(a)] transforms to a point source in the slab frame [32,33] [Fig. 1(b)] which then excites a plasmonic surface wave. The surface SH source resulting from those FF fields can be calculated and transformed back to the TW frame, as discussed in detail in [2,26,34]. It has the generic form

$$J_{z,r}(x, y) = \frac{\chi_{S,\perp\perp\perp}^{(2)}}{\varepsilon_{bg}^{2\omega}} \partial_\parallel (E_\perp^\omega E_\perp^\omega) \delta(x^2 + y^2 - 2ax), \quad (1)$$

where x and y are the spatial coordinates, a is the wire radius [see Fig. 1(a)], $\chi_{S,\perp\perp\perp}^{(2)}$ is the surface second-order susceptibility perpendicular to the interface, $E_\perp^\omega$ is the FF electric field perpendicular to the wire interfaces, and $\varepsilon_{bg}^{2\omega}$ is the background permittivity at the SH.

Second, this solution revealed why the SH field profile is quadrupolar and antisymmetric [see Fig. 1(c)]: The FF modes excited in the slab frame have electric fields that are

---

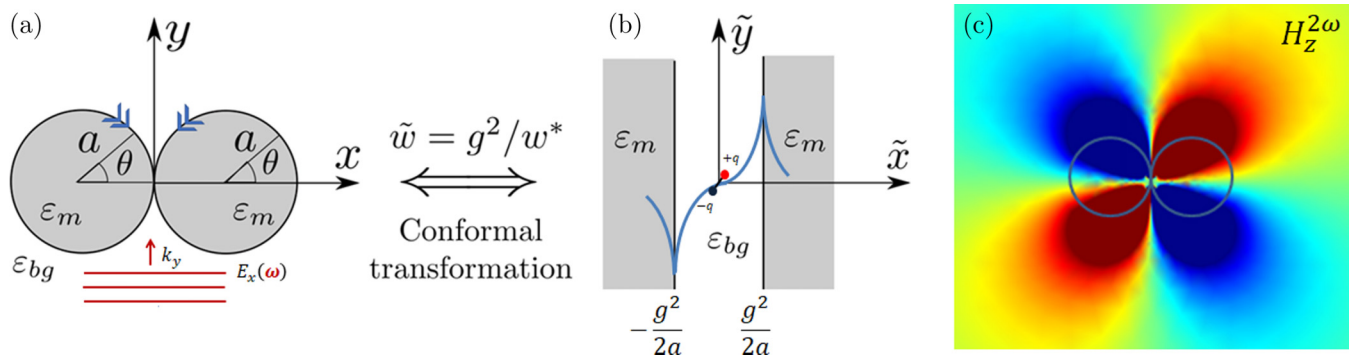*elshimon@post.bgu.ac.il
†kothakap@post.bgu.ac.il

FIG. 1. Schematics of (a) the (identical) touching wire system and (b) the slab geometry to which it is related via an inversion transformation. (c) The scattered second-harmonic magnetic field; a quadrupolar pattern with distinct antisymmetry in both x and y is observed.

symmetric in x and y, since these are the surface-plasmon waves that exist within the frequency band below the plasma resonance frequency (see [26]). The square of the FF electric field in (1) is symmetric, but the differentiation operator causes the source to be antisymmetric in x and y, so it excites the higher frequency asymmetric slab mode via the so-called mode matching (MM) condition [implicit in Eq. (A1); see [26]] [see Fig. 1(b)]. Transforming back to the TW frame yields the observed profile.

Third, the TO solution (A1) revealed that the magnitude of the SH field is proportional to three factors. The first factor is the strength of the SH source, $J_{z,r}$ (1). The second factor is the magnitude of the so-called phase-matching (PM) parameter

$$\mathcal{P}(\omega) = \cosh(2\alpha^\omega) + \frac{\varepsilon_{bg}^{2\omega}}{\varepsilon_m^{2\omega}} \sinh(2\alpha^\omega), \qquad (2)$$

where α^ω is the propagation constant as well as the mode transverse width. $\mathcal{P}(\omega)$ represents the pole of the dispersion relation of the antisymmetric slab mode, i.e., the proximity to the SH resonance of that mode. The third factor is a newly identified geometric factor [see (A4) which originates from the nonuniform distributed nature of the source across the metal-dielectric interface and suppresses SHG from the touching point]. Further details on the physical interpretation of these terms and explanations of the parameters on which they depend are supplied in Appendix A.

In the present paper, we proceed beyond [26] by exploiting the analytic solution (A1) and the qualitative insights it provides to perform a *quantitative* study of the SHG from the TWs. Specifically, we study the interplay between the three aforementioned factors to *optimize* the near-field enhancement, but now also the far-field response, as quantified by the scattered power at the SH wavelength, $P_{\text{scat}}^{2\omega}$.

The paper is organized as follows. In Sec. II, we describe the configuration under study and the methodology. In Sec. III, we compare the SH response of the TWs with that of a single wire, demonstrating up to six orders of magnitude greater SHG efficiency. In Sec. IV, we explore how the SHG of the TWs varies with ε_{bg} and show that the scattered power can be increased by even ten orders of magnitude by increasing ε_{bg}. In Sec. V, we analyze the spectral response and identify the origins of its narrow-band nature. In the last section of the paper, we exploit our analytic solution of a

nontrivial nanophotonic geometry as a platform to perform a critical comparison of the strengths, weaknesses, and validity of other prevailing theoretical approaches employed for nonlinear wave interactions at the nanoscale. Finally, we conclude with an outlook.

II. CONFIGURATION AND METHODOLOGY

For all results presented in this paper, we choose a wire radius of $a = 5$ nm, with a permittivity characterized by a Drude model (with parameters suitable for Ag, namely, $\varepsilon_\infty = 5$, $\omega_p = 9.2$ eV, and $\gamma = 0.2$ eV [35]). We also choose $\chi_{S,\perp\perp\perp}^{(2)} = 10^{-20}$ m²/V in all simulations. However, all SH results in this paper are linearly proportional to this parameter, so it can be adjusted to suit any particular nonlinear polarization model. We perform calculations for two dissipationless background permittivities: low ($=1$, considered previously in [26]) and high ($=12$, characterizing semiconductor materials with negligible losses, i.e., when illuminated at a frequency lower than the energy band gap of the semiconductor). For simplicity, we also assume the host to be dispersionless (i.e., $\varepsilon_{bg}^{2\omega} = \varepsilon_{bg}^\omega = \varepsilon_{bg}$). To ensure a fair comparison, we choose the incident FF field to be an x-polarized (i.e., along the dimer axis) plane wave with unit amplitude in both cases. H field values are thus given in relative units.

We discuss below three main types of results. We first focus on the near-field SH wave along the perimeter of the wire, marked by C. Due to symmetry, we consider only the right wire of the TWs. This $H_z^{2\omega}$ field is given by (Appendix A)

$$H_z^{2\omega}(x, y)|_C = -i\omega\varepsilon_0\varepsilon_{bg}^{2\omega}\frac{\sinh 2\alpha^\omega}{2\alpha^\omega\mathcal{P}} x J_{z,r}(x, y). \qquad (3)$$

This demonstrates that the resulting $H_z^{2\omega}$ at each point is proportional to $J_{z,r}$ at that point, subject to the two aforementioned additional factors. These are the PM parameter defined in (2), and the geometric factor (A4), which has been reduced to x along the TW perimeter. Note that in the plots below we show only the region relatively close to the touching point, as it is the most interesting, informative, and influential regime.

We also present the scattered power; the details of its analytic and numeric calculations are given in Appendix B. Finally, in the context of the spectral response, we also present various averaged values of near-field properties over the TW
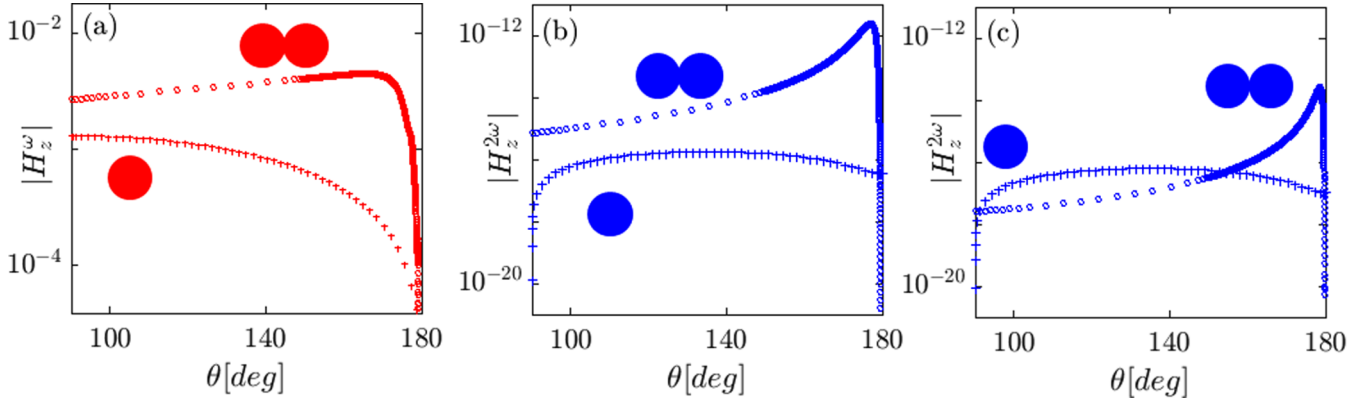
FIG. 2. (a) The numeric solution for the absolute value of the (scattered) linear magnetic field $|H_z^\omega|$ along the perimeter of the TWs ($\circ$) and the single wire ($+$) as a function of angle θ for $\varepsilon_{bg} = 12$ at a fundamental wavelength of 922 nm (hence, $\lambda_{SH} = 461$ nm). (b) Same as (a) for the SH magnetic field $|H_z^{2\omega}|$. (c) Same as (b) at a fundamental wavelength of 1400 nm. The case of $\varepsilon_{bg} = 1$ is qualitatively similar (data not shown). In all cases, the incident electric field is an x-polarized plane wave with unit amplitude.

perimeter, defined as

$$\langle |f(x,y)| \rangle_C = \frac{1}{4\pi a} \int_C |f(x,y)| \, dx \, dy. \qquad (4)$$

As observed in [26], the source $J_{z,r}$ (1) and magnetic field (3) were found to be in excellent agreement with the numeric solution only relatively close to the touching point [36], and not too close to PM. Therefore, whenever we discuss the solution far away from the touching point, we employ the numeric (COMSOL-based) solution instead of the analytic one (e.g., for scattering calculations). As is customary, analytic results are marked by lines, and numerical results by symbols. Further, in order to distinguish the FF and SHG results, all SHG data are displayed in blue, and all FF are displayed in red, in line with their relative spectral position.

III. SINGLE WIRE VS THE TOUCHING WIRES

As an initial step, we compare the (scattered) SH fields of the touching wires and a single wire. Overall, the single wire near field varies sinusoidally along the wire perimeter. As can be shown from (cylindrical) Mie analysis [34,37,38], under the (x-polarized) FF plane-wave illumination, all the modes excited in the wire vanish at $\theta \to \pi$ (the would-be touching point of the TWs), but only the modes having even azimuthal indices ($M = 2, 4, \dots$) vanish at $\theta \to \pi/2$, thus giving rise to a finite field, as seen in Fig. 2(a). At the SH wavelength [Figs. 2(b) and 2(c)], the situation is inverted, namely, all the modes excited in the wire vanish at $\theta \to \pi/2$, but only the modes having even azimuthal indices vanish at $\theta \to \pi$.

The TW fields exhibit radically different behavior than the single nanowire (both for the FF and SH wavelengths); they focus near the touching point [39], and then decrease rapidly towards touching point $\theta \to \pi$. Near the resonances [i.e., at the FF resonance, Fig. 2(a) or the SH resonance, Fig. 2(b)], the TWs generate stronger SH near fields for essentially all incidence angles due to the intrinsic singular character of the geometry. Figure 2(c) demonstrates the situation for illumination further from resonance (i.e., for a longer wavelength). Here, the TWs generate a stronger near field close to the touching point only.

The behavior of the scattered power is somewhat more complicated. As shown already in [32,33], Fig. 3(a) shows that the single wire exhibits stronger linear (i.e., at the FF) scattering compared with the TWs when both systems are at resonance [40]. However, since the spectral bandwidth of the TW response is much wider, the TW response is stronger away from resonance. Surprisingly, the situation is inverted for the SH scattered power, as seen in Fig. 3(b). In particular, the power scattered at resonance by the TWs is greater by more than six orders of magnitude. Yet, since its spectral width turns out to be significantly narrower, the power scattered at longer wavelengths is greater for the single wire. This is the first main result of the current work; it is further elaborated in Sec. V below. This behavior can be traced to the relatively weak SH fields generated at points along the TW perimeter further from the touching point in the off-resonance case [see Fig. 2(c)] as it is these points that determine the far-field scattered power [see Fig. 7(a) and further discussion in Appendix B].

Also worth noting is that the peaks of FF and SH scattered powers are at the same wavelength for the single nanowire, and these coincide with the peak of the TW linear response. However, the peak SH response of the TW is blue-shifted. The origin of this blue-shifting can be understood from the modal information revealed by TO. In particular, all plasmonic modes lie exactly at the surface-plasmon frequency for the single nanowire in the quasistatic limit adopted in the current study; indeed, this configuration corresponds to a single interface plasmonic waveguide in the transformed slab frame. This corresponds to ~580 nm (see Fig. 3) for which $\mathrm{Re}[\varepsilon_m] \approx -12$. However, for the TWs [which transform to the slab waveguide, Fig. 1(b)], two branches emerge in the dispersion relation, one above and one below the surface-plasmon frequency. The upper branch corresponds to the antisymmetric modes, and is characterized by a negative group velocity. As a result, the modes corresponding to smaller wave vectors (i.e., those which correspond to the quasistatic limit) have the highest frequency and the wider spatial extent; the latter corresponds to the highest radiative damping. A more detailed discussion as well as a visualization can be found in [41]. Since the SH field is asymmetric [see Fig. 1(c)], the SH peak
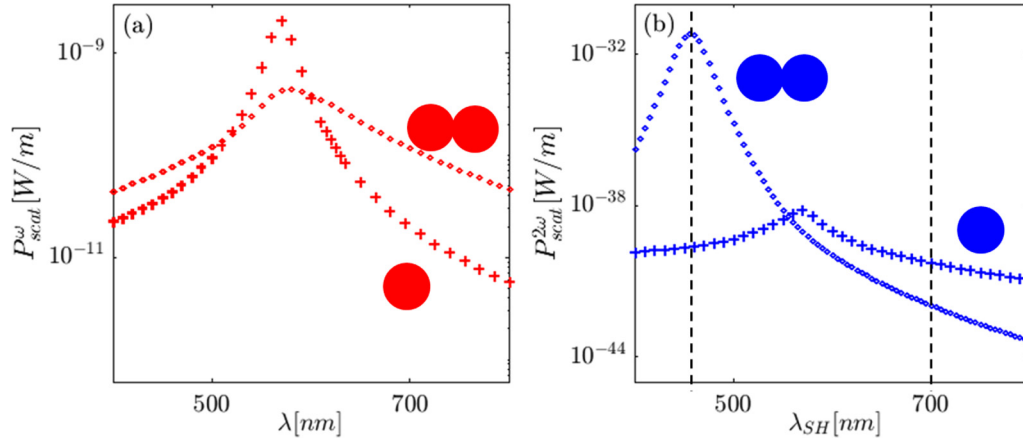
FIG. 3. (a) The numeric solution for the linear (i.e., at the FF) scattered power of TWs (+) and single wire (○). (b) The corresponding solution for the SH scattered power; the black dashed lines represent the scattered power for fundamental wavelengths 922 and 1400 nm, corresponding to the near-field plots in Figs. 2(b) and 2(c). Both scattered powers are calculated for $\varepsilon_{bg} = 12$.

of the TWs occurs at frequencies that correspond to the higher frequency branch, above the surface-plasmon frequency and approaching the metal plasma frequency.

IV. OPTIMIZATION OF THE SH RESPONSE OF THE TOUCHING WIRE

The analytic solutions for the near and far fields now allow us to scan the parameter space in search of the optimal response, by varying ω, ε_{bg}, etc. While this has clear practical value, it is also tedious, and is worth doing only for a well-defined experimental setup. Instead, we opt to explain these findings qualitatively, and to identify the governing physics that enable further optimization of the SH response. In particular, we exploit the solution (A1) and analyze the contributions of the previously mentioned factors to the SH response. A link exists between the near-field and far-field behavior realized by $\mathcal{R}$ (A2) [see Fig. 7(a) and Appendix B], so it suffices to analyze the near-field solution (3).

A. Near-field response

We now analyze the SH generation efficiency by evaluating each of the various elements in Eq. (3) separately. We begin by finding the optimal material parameters for which the phase-matching factor $1/|\mathcal{P}|$ is maximized [42], i.e., the background permittivity and frequency that brings the system as close as possible to phase matching (or equivalently, to SH resonance). From Fig. 4(a), it is evident that the background permittivity required to maximize $1/|\mathcal{P}|$ is high, especially as the fundamental wavelength gets longer. For example, for a fundamental wavelength of 922 nm (hence, $\lambda_{SH} = 461$ nm), the optimal choice for the background dielectric is ≈ 12 [marked by the top "○" symbol in Fig. 4(a)]; this motivates *a posteriori* the choice of parameters in the previous section. Figure 4(a) also shows an overall moderate sensitivity of $1/|\mathcal{P}|$ to the choice of permittivities and SH wavelength. In particular, the high permittivity case yields a maximum value of $1/|\mathcal{P}| \approx 3.2$ for $\varepsilon_{bg} = 12$, whereas $1/|\mathcal{P}| \approx 1$ for the $\varepsilon_{bg} = 1$ case.

We now turn to study the effect of ε_{bg} on the product of the surface source with the geometric factor, namely, $xJ_{z,r}$. To do so, we first display in Figs. 5(a) and 5(b) the real and absolute value of the FF fields $E_\perp^\omega$ along the wire perimeter for both choices of ε_{bg}. The maxima of the fields are roughly of the same order of magnitude for both cases. While both maxima are located close to the touching point, the maximum for $\varepsilon_{bg} = 12$ is found further from the touching point, corresponding to smaller angles. Indeed, it was shown in [33] that the position of the peak value of the FF fields can be approximated by

$$\theta_{\max}^\omega \cong \pi - \frac{\mathrm{Im}\left(\frac{\varepsilon_m^\omega}{\varepsilon_{bg}}\right)}{\left|\frac{\varepsilon_m^\omega}{\varepsilon_{bg}}\right|^2 - 1}, \tag{5}$$

where $\theta_{\max}^\omega$ is the angle measured along the perimeter of the right wire. Relatively low losses were assumed [specifically, $\mathrm{Im}\left(\frac{\varepsilon_m^\omega}{\varepsilon_{bg}}\right) \ll \left|\frac{\varepsilon_m^\omega}{\varepsilon_{bg}}\right|^2 - 1$]. This shows that when the FF approaches the plasmon resonance, the peak position of the linear fields approaches $\theta \to 0$. Conversely, for longer wavelengths the linear electric field, and hence the source term at SH, are pushed more towards the touching point, and the attenuation due to the geometric factor increases [compare, e.g., Figs. 2(b) and 2(c)] [43]. In particular, it follows from Eq. (5) that since the value attained by $|\varepsilon_m^\omega/\varepsilon_{bg}|^2 - 1$ is much smaller for $\varepsilon_{bg} = 12$ than for $\varepsilon_{bg} = 1$, then, $\theta_{\max}^\omega$ is found further away from the touching point for $\varepsilon_{bg} = 12$. For a complete map of the $\theta_{\max}^\omega$ dependence on the SH wavelength and background permittivity, see Fig. 4(b).

Recall now that the SH source $J_{z,r}$ is computed by squaring the FF fields and evaluating the tangential derivative along the perimeter of the TW. Thus, faster oscillations give rise to a stronger SH source. Those are observed for the lower background dielectric case [with a shorter wavelength resonance; see Fig. 4(a)]. This phenomenology is the same as reported for increasing frequency and fixed background [44]: as the frequency gets further away from the surface-plasmon resonance, the field oscillation becomes faster. Here, this happens because the growing background permittivity effectively shifts the plasmon resonance to the red. Indeed, Figs. 5(c)
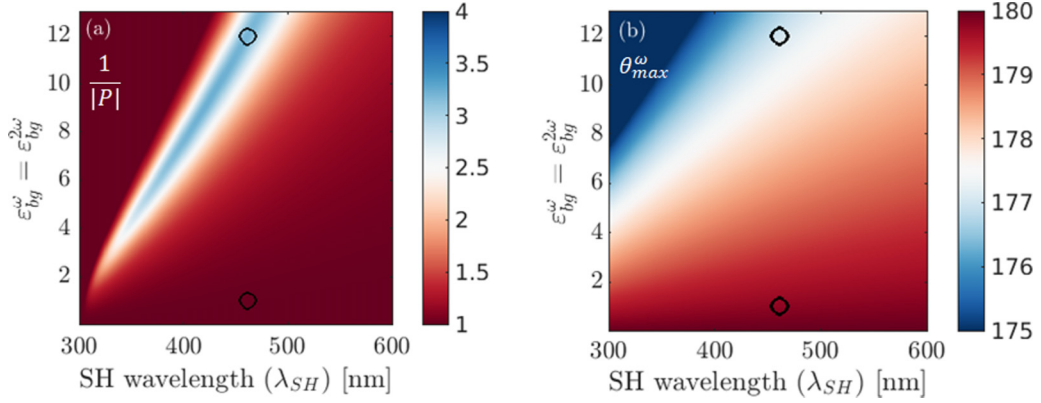
FIG. 4. (a) $1/|\mathcal{P}|$ (2) as a function of SH wavelength and dispersionless dielectric background ε_{bg}. The points marked "○" denote simulations at the SH wavelength of 461 nm, for $\varepsilon_{bg} = 12$ and $\varepsilon_{bg} = 1$. (b) $\theta_{\max}^{\omega}$ [see Eq. (5)] as a function of SH wavelength and dielectric background ε_{bg}.

and 5(d) show that the faster oscillations associated with the $\varepsilon_{bg} = 1$ yield a 15-fold stronger source term.

Yet, the complete SH response (namely, $xJ_{z,r}$) is much stronger for the $\varepsilon_{bg} = 12$ case, as seen in Fig. 5(e). This is the effect of the geometric factor [see Eqs. (3) and (A4)]. It acts to suppress the SHG of the $\varepsilon_{bg} = 1$ case more effectively compared with the $\varepsilon_{bg} = 12$ case because of the closer proximity of the field peak to the touching point. Specifically, the

peak value of the SH response (3) is 32 times higher for the $\varepsilon_{bg} = 12$ case, due to the combined effect of an approximately ten times stronger maximum value of $|xJ_{z,r}|$ (compared to the 15-fold lower maximum value of the source only) and an $\sim$3.1-fold higher value of $1/\mathcal{P}$.

Thus, our analysis reveals that having a stronger SH source *does not* guarantee a stronger SH response, a potentially counterintuitive result that stands in contrast to the
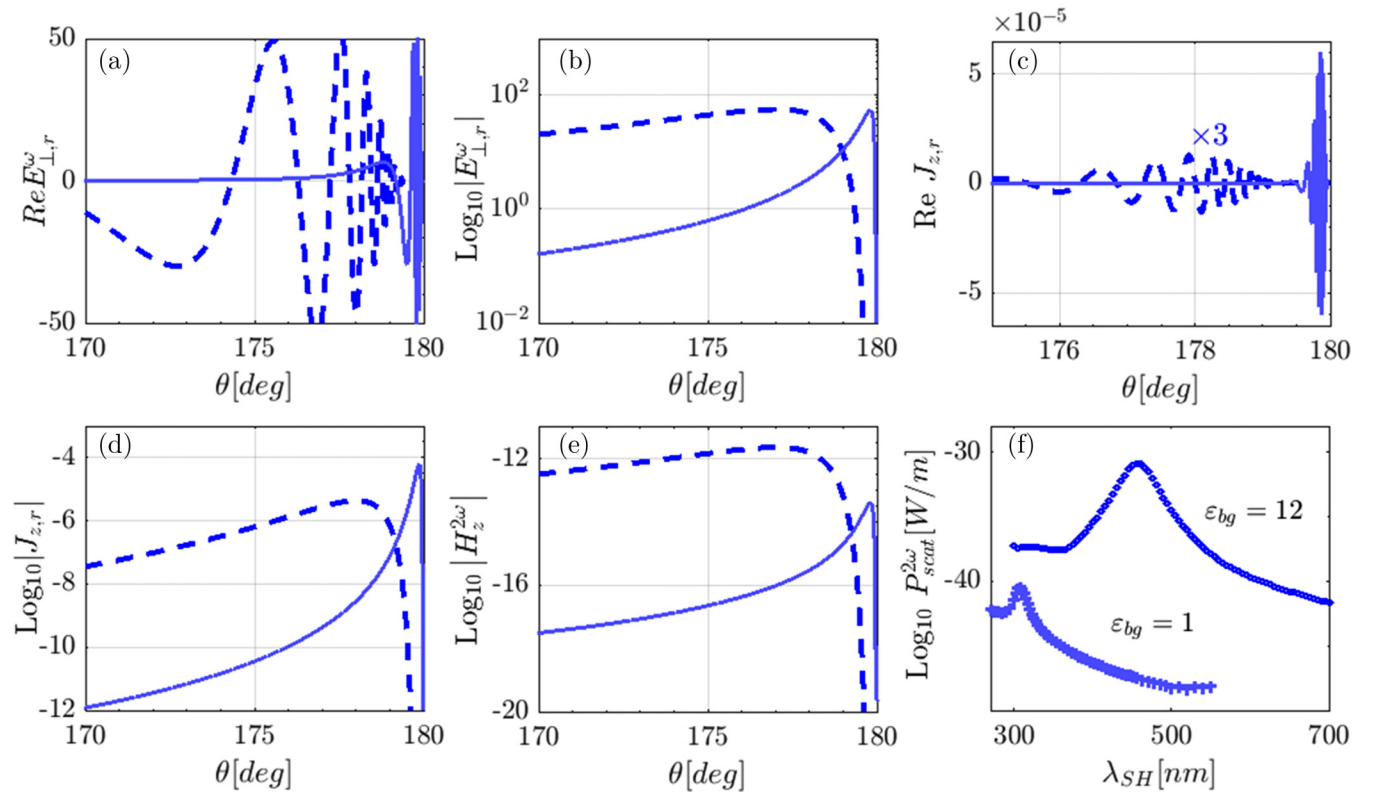

FIG. 5. (a)–(e) Analytic solutions of near fields. Fields are plotted as a function of angle θ (see Fig. 1) along the perimeter of the right wire for the TW system. Curves for $\varepsilon_{bg} = 1$ and $\varepsilon_{bg} = 12$ are plotted using light-blue solid lines and dark-blue dashed lines, respectively, and in slightly different colors. Note the particularly rapid oscillations in the former case. Linear fields (a) $\mathrm{Re}[E_{\perp}^{\omega}]$ and (b) $|E_{\perp}^{\omega}|$ at the FF wavelength 922 nm. The SH source (c) $\mathrm{Re}[J_{z,r}]$ and (d) $|J_{z,r}|$ at the SH wavelength of 461 nm. (e) The SH magnetic field $H_z^{2\omega}$, where the curve of $\varepsilon_{bg} = 12$ is threefold magnified. (f) The numeric solution for the SH scattered power of TWs for $\varepsilon_{bg} = 12$ (dots) and $\varepsilon_{bg} = 1$ (crosses).

predictions of approximate models [11,17]. Instead, it is the spatial distribution of the SH source, i.e., the product $xJ_{z,r}$, that determines the near-field SH response.

Overall, we have seen that high permittivity values are beneficial for increasing both the PM factor (2) as well as the spatial distribution of the source, $xJ_{z,r}$, at least within the regime where Eq. (5) is valid. One might then ask what would be the ideal choice of the background permittivity for an optimal SH near-field response. The strongest source would be achieved at the FF surface-plasmon resonance, $\varepsilon_{bg} \approx -\text{Re}[\varepsilon_m^\omega]$. Such a choice would also serve to pull the source maximum away from the touching point [see Eq. (5)] such that the SH near field becomes stronger. On the other hand, a maximal value of $1/|\mathcal{P}|$ corresponds to a different value, namely, the permittivity at the SH plasmon resonance wavelength, i.e., $\varepsilon_{bg} \approx -\text{Re}[\varepsilon_m^{2\omega}] \neq -\text{Re}[\varepsilon_m^\omega]$. A signature of the contradicting nature of these requirements can be seen in Fig. 4.

Thus, improving the SH response by taking the geometric factor and phase-matching condition simultaneously into consideration demands the illumination be doubly resonant, i.e., at both FF and SH. Such a scenario was demonstrated in [16,23,24] and involved nontrivial particle geometries. For the structure studied here, which is characterized by a single resonance, optimal performance can be achieved via a maximally wide resonance bandwidth such that the system can satisfy both requirements.

B. The far-field response

The discussion so far focused on the near fields along the segment of the perimeter closest to the touching point. We turn now to the far fields. As discussed in Appendix B (see Fig. 7), its strength is determined by the values of $J_{z,r}$ on the perimeter further from the touching point, corresponding to the smaller angles displayed in Figs. 5(d) and 5(e). In this regime, the effects of the geometric factor discussed in Sec. IV A are essentially irrelevant. Instead, it is the decay length of the fields away from the touching point that determines the far-field response. This decay is slower for the $\varepsilon_{bg} = 12$ case [see Figs. 5(b) and 5(d)] so that indeed, the far-field response in that case is much stronger. In particular, the source term for the $\varepsilon_{bg} = 12$ case at angles away from the touching point is about five orders of magnitude greater than for $\varepsilon_{bg} = 1$. This originates from the fact that the FF electric field in the source term is approximately two orders of magnitude higher for the $\varepsilon_{bg} = 12$ case [see Fig. 5(b)] due to the proportionality to the background permittivity and to α^ω (which represents field confinement and the propagation constant) [see Eq. (3)]. Both of these are higher by an order of magnitude for the $\varepsilon_{bg} = 12$ case. The differentiation of Eq. (1) extracts a further factor of α^ω, hence adding another order of magnitude. This result was obtained in [33]; again, its significance was not emphasized, yet, its origins were. Indeed, only the ratio between permittivities appears in quasistatic expressions in [33] such that increasing the permittivity in the background is equivalent to reducing the absolute value of the metallic one. As a result, the highest confinement takes place at large, negative values of the metal permittivity (i.e., at long frequencies of a Drude metal) or for high permittivity background. As explained in

Sec. V below, this behavior also explains the spectrum of the scattered SH power.

As a result, the scattered power (which scales with the square of the fields) is about ten orders of magnitude greater for $\varepsilon_{bg} = 12$ than for $\varepsilon_{bg} = 1$ [see Fig. 5(f)]. This is the second main result of the current work. It is particularly remarkable in comparison to the single wire, where a change in ε_{bg} improves the scattered power by "only" two orders of magnitude (not shown). Sections IV A and IV B have demonstrated that the $\varepsilon_{bg} = 12$ case exhibits superior behavior both in the SH near- and far-field regimes of the TWs.

V. THE SH SPECTRAL RESPONSE OF THE IDENTICAL TOUCHING WIRES

From the analysis of Sec. IV A, it became clear that one way to optimize the SHG efficiency of the TWs is to increase the bandwidth of its spectral response. In fact, the unusually large bandwidth of the linear response of the TWs [32,33] was also our original motivation to study SHG from the TWs. Moreover, a further increase in the SH bandwidth was expected due to the effects of autoresonance, also known as adiabatic frequency conversion [45]. This was demonstrated in tapered dielectric waveguides [46], and relied on sweeping the phase-matching parameter (analogous to $\mathcal{P}$) adiabatically through zero along the propagation direction instead of achieving the exact phase matching within the entire nonlinear medium. Since the tapered waveguide is mimicked by the TW geometry near the touching point for the modes circulating around the particle perimeter [e.g., Fig. 1(a)], a similar wide SH bandwidth was expected. Unfortunately, as we shall see below, the SH response of the TWs did not meet such expectations. Instead, the response turned out to be narrow band, as it typically is.

To understand why, we plot the key physical quantities in solution (3) against the fundamental and second-harmonic wavelength, spatially averaged over the TW perimeter [see (4)] for $\varepsilon_{bg} = 1$ [Fig. 6(a)] and $\varepsilon_{bg} = 12$ [Fig. 6(b)], respectively, and compare them to the PM factor [Fig. 6(c)].

We first consider the spectral behavior of the SH source. It is obtained by squaring the FF field, so that the spectral bandwidth of the SH source is necessarily narrower than the linear response [compare the red and magenta curves in Fig. 6(a); the effect is less pronounced in Fig. 6(b)]. Further limitation on the bandwidth is imposed by the geometric factor x [see green curves in Figs. 6(a) and 6(b)]. Indeed, one might naively conclude that this term is insignificant in determining the spectral response as it is only a spatial factor that remains unchanged regardless of wavelength, but Eq. (5) and Fig. 4(b) show that the opposite is true. Indeed, the geometric factor is less harmful near the SH resonance; this is due to the wavelength dependence of the maximal field position [see the discussion surrounding Eq. (5)]. Thus, the geometric factor plays a significant role, and determines not only the near-field enhancement [see Fig. 5(e)], but also the spectral bandwidth of the SH near fields [47]. In contrast, Fig. 6(c) shows that the peak position is determined by the PM factor (2).

Finally, we observe that both the far-field and near-field responses peak at the same wavelength, yet the bandwidth of the far-field response is significantly narrower [compare
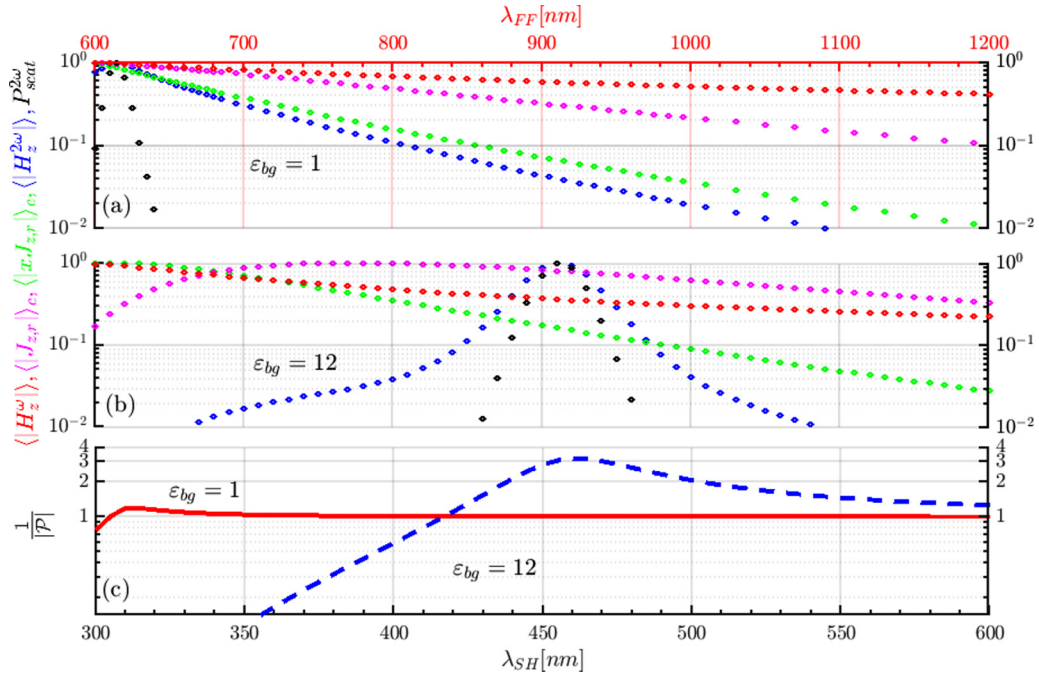
FIG. 6. Spectral responses of the SH near field of the identical TW system. Normalized average of the near-field quantities along the perimeter of the TW, namely, $\langle|H_z^\omega|\rangle$ (red dots), $\langle|J_{z,r}|\rangle$ (magenta dots), $\langle|xJ_{z,r}|\rangle$ (green dots), $\langle|H_z^{2\omega}|\rangle$ (blue dots), and $P_{scat}^{2\omega}$ (black dots) for (a) $\varepsilon_{bg} = 1$ and (b) $\varepsilon_{bg} = 12$. Each curve is normalized by its maximum value in the spectral range of interest. (c) The PM factor $1/|\mathcal{P}|$ (2) as a function of SH wavelength for $\varepsilon_{bg} = 1$ (solid red line) and $\varepsilon_{bg} = 12$ (dashed blue line).

black and blue curves in Figs. 6(a) and 6(b)]. This difference can be understood by recalling that the spectral width of far-field resonances is governed by radiative damping, whereas absorption losses dominate the near field. The latter are much faster than the former for small particles roughly a few tens of nanometers in radius like the ones considered in our study [48]. This well-known effect provides further spectral narrowing on top of that caused by the geometric factor.

These results show why, contrary to expectations, the bandwidth of the SH response is much more limited than the linear response. In retrospect, the TO approach reveals that although the geometry we study resembles a tapered waveguide, it is fundamentally based on the flat slab geometry, for which no autoresonance response is expected. This unexpected insight is most likely unique to tapered geometries that are related by TO to nontapered ones; further research is required to clarify this point.

VI. COMPARISON TO PREVIOUS WORK AND OUTLOOK

The goal of the current work was to highlight the utility of TO as a tool for the interpretation of the wave physics of nonlinear optical wave interactions in plasmonic nanostructures, and the optimization of its performance. This was demonstrated by a thorough analysis of a well-studied singular plasmonic structure—the TWs—using the simplest possible solid-state model for the second-order optical response of metals.

The combined near- and far-field analyses provided in this work enables comparison with some commonly used theoretical approaches employed for SHG in nanostructures. To

perform this comparison, we first recall that the exact formal solution for the SHG problem from an arbitrary scatterer is simply the convolution of the SH current with the Green's tensor $(\overleftrightarrow{G})$, which represents the response of the structure to a point dipole source (i.e., the spatial impulse response of the scatterer); it is generically a complicated function of space and frequency. Our analysis of the TWs showed that some aspects of the far-field response, such as the permittivities that yield stronger SH responses, can be correctly predicted by considering only the nonlinear polarization (i.e., the source, J_z), Figs. 5(d) and 5(f), i.e., regardless of the details of $\overleftrightarrow{G}$. This approach is essentially Miller's rule, which is applicable to bulk materials that exhibit a relatively weak spectral sensitivity, and involves fairly uniform fields (i.e., no complex scattering due to subwavelength structuring). In this case, the Green's tensor too exhibits weak variations in space and frequency, such that the general far-field solution is indeed simply proportional just to the SH source. This polarization-based model was also shown to be successful when applied to systems far from resonance, as, e.g., in [18], or those that have a relatively broad FF resonance, as in the current case [see Figs. 4(a) and 6(a)].

However, our solution shows that the *near* field exhibits a more complicated form. It includes considerations such as the proximity to the SH resonance (which we refer to as PM) and symmetry of the source and modes (via the more quantitative concept of MM). These considerations arise naturally in the so-called nonlinear scattering/effective susceptibility model [11,19] whereby the product of the SH polarization with the linear field is spatially averaged. This approach was shown to predict correctly various additional quantitative aspects of the solution (e.g., the optimal structural asymmetry [19]).

Yet, the nonlinear scattering/effective susceptibility model does not accurately handle the interplay between the SH source ($\sim J_{z,r}$) and the SH response ($\sim \overleftrightarrow{G}$), in that it does not rely on the exact Green's tensor of the structure [49], instead relying on the profile of an incident plane wave. Moreover, it does not correctly account for the convolution between these two quantities, instead relying on their product. The former approximation may yield discrepancies in the spatial and spectral responses while the latter approximation can lead to somewhat different interference effects compared with straightforward averaging [11]. It is clear that these effects did not prevent the good agreement between analysis and measurement in the far-field response reported by [19], but it may not correctly predict the near field [11]. Since our exact solution is free of the approximations adopted in the nonlinear scattering theory of [11], it indeed predicts a near-field behavior that differs from the far field, as seen in Figs. 3–5. In our specific case, this is due to the appearance of the geometric factor, which modifies the near-field enhancement [see Fig. 5(e)], and controls the overall bandwidth of the spectral response (see Fig. 6). All the above shows that polarization-based models such as Miller's rule or simplified models such as the nonlinear scattering model/effective susceptibility model [11,19,50] should be used with caution in structured nanophotonic systems. Nevertheless, these simpler models are applicable to a wide class of systems, while it is not clear how the additional insights revealed in our work apply to other structures.

In addition to the above, we emphasize that the discussion in the current work should not be construed as anything more than a qualitative study. Indeed, various effects are expected to modify the quantitative results shown here, such as nonlocality [44,51], dispersion of the second-order response (which is not yet fully understood, in general), interband transitions [52], etc. These may modify the near-field enhancement and spectral response. Nevertheless, the analytic solution and insights obtained in this work can lead towards various ways of improving the response quantitatively; for example, it can reveal the material dispersion or anisotropy of the background medium necessary for the optimal response. More significant improvements may be achieved if the background also has a second-order optical response; this is particularly likely for the high permittivity background which was found to yield superior performance in this study. In that sense, it would be interesting to build on recent work on SHG from such systems [53–56], and to study the relative importance of the SHG from each material.

In addition to its insights on the TWs, the current study can be extended to a variety of additional plasmonic nanostructures. Specifically, one can exploit the results for

dipole sources above a metal layer in [57] to study the field distribution due to illumination by electric fields of different polarizations as well as to study other configurations such as the crescent structure [58], nontouching wires [59], blunt geometries [60], periodic arrays, two-dimensional materials [61,62], and various three-dimensional structures [63,64], etc. Future steps may include further optimization of the performance, e.g., by exploiting the greater susceptibilities reported within heterodimers [9,10] or even to treat more complicated nonlinear wave interactions such as sum frequency generation [65,66], third-harmonic generation [18,19,67], terahertz generation [65,68], and four-wave mixing [69].

Finally, our study will hopefully motivate an experimental test of our predictions. Indeed, many aspects of the linear response of TWs revealed by earlier analysis were already experimentally demonstrated using thin disks (in the terahertz regime; see [70,71]).

APPENDIX A: THE ANALYTIC SOLUTION FOR THE SH MAGNETIC FIELD NEAR THE TOUCHING WIRES

In [26], we calculated the SH field generated by a pair of (identical) TWs (Fig. 1) assuming the simplest second-order nonlinear polarization of the metal, i.e., assuming it is dominated by a perpendicular *surface* source. As explained in [2,26,34], this is a reasonable generic (even if not complete) description of the second-order nonlinear optical response of metals; indeed, *bulk* polarization can also be accounted for by mapping it to a surface polarization. We showed that a highly accurate analytic solution can be obtained in three steps. First, we transformed the SH source [72] (calculated within the quasistatic approximation [32,33]) and boundary conditions to the slab frame (see Fig. 1) using a conformal inversion transformation [32]. Then, by assuming that the amplitude of the excited guided wave in the slab geometry is slowly varying along $\tilde{y}$, we imposed the boundary conditions appropriate for the surface source (namely, continuity of the magnetic field and proper discontinuity of the parallel electric field [34]) [73]. Finally, we transformed back to the TW frame and obtained

$$
H_z^{2\omega} = \frac{-i\omega\varepsilon_0}{2\alpha^\omega \mathcal{P}(\omega)} \mathcal{R}(\tau_x, \tau_y) \mathcal{G}(x, y) \exp\left(\frac{4ia\alpha^\omega y}{x^2 + y^2}\right)
$$

$$
\times \begin{cases} \sinh\left(\dfrac{4a\alpha^\omega x}{x^2 + y^2}\right), & x^2 + y^2 + 2a|x| > 0 \\[3mm] \mathrm{sgn}[x]e^{2\alpha^\omega}\sinh 2\alpha^\omega \exp\left(\dfrac{-4a\alpha^\omega |x|}{x^2 + y^2}\right), & x^2 + y^2 + 2a|x| < 0. \end{cases} \tag{A1}
$$

Here, x and y are the real-space coordinates; $\alpha^\omega = \frac{1}{2}\ln(\frac{\varepsilon_m^\omega - \varepsilon_{bg}^\omega}{\varepsilon_m^\omega + \varepsilon_{bg}^\omega})$ is the dimensionless [74] propagation constant at the fundamental frequency ω; ε_{bg}^ω, ε_m^ω, and ε_0 are the background, metal, and vacuum permittivities, respectively; a is the wire radius; and $\mathcal{P}$ (2) is the so-called PM factor. It represents the pole of the dispersion relation of the antisymmetric mode. It is maximal at resonance, i.e., when the SH frequency is tuned to the frequency of that mode [26,75]. $\mathcal{R}$ is related to $J_{z,r}(x, y)$, the (z-directed) surface magnetic current generated by the nonlinear polarization on the right wire. It is evaluated via the analytic solution for the FF fields, $E_\perp^\omega$, provided in [33], and is itself given by Eq. (1) such that $\mathcal{R}$ is defined via

$$J_{z,r}(x, y) = \mathcal{R}(\tau_x, \tau_y) \exp\left(\frac{4ia\alpha^\omega|y|}{x^2 + y^2}\right)\delta(x^2 + y^2 - 2ax). \tag{A2}$$

Here, the coordinates τ_x and τ_y are defined as

$$(\tau_x, \tau_y) = \left(\frac{1/(2a)}{1/(4a^2) + y^2/(x^2 + y^2)^2}, \frac{y/(x^2 + y^2)}{1/(4a^2) + y^2/(x^2 + y^2)^2}\right). \tag{A3}$$

These coordinates map points in the domain outside the TWs to the TW perimeter [see Fig. 7(a)]. Finally, the factor

$$\mathcal{G}(x, y) = \frac{4a(x^2 + y^2)^2}{4a^2y^2 + (x^2 + y^2)^2} \tag{A4}$$

is referred to as the geometric factor. It originates from a transformation of the generalized boundary condition (which incorporates the discontinuity in the tangential electric field) to the slab geometry [26] as well as from the complex nonuniform distributed nature of the source. Along the TW perimeter, $\mathcal{G}$ reduces to simply x, as shown in [26]; this is used in Eq. (3).

APPENDIX B: SCATTERED POWER CALCULATIONS

Scattered power is probably the most accessible observable in experimental studies of small nanoparticles. However, it vanishes in the quasistatic limit, which was the limit used to calculate the linear electric fields [32,33]. Previous works (e.g., [76]) went beyond this limit by computing the linear absorption and scattering cross sections of the TWs based on the dipole moment induced by the incident fields. As in the case of the near-field enhancement, the TWs exhibited a scattering cross section which is spectrally much broader compared to the single wire. Hence, it is interesting to see if a large bandwidth is obtained also for the SH response.

Unfortunately, the approach of [76] cannot be applied in our case, as a total SH dipole moment cannot be defined for the nanostructure at the SH. Instead, we exploit the inherent near-to-far-field mapping which is manifested by $\mathcal{R}(\tau_x, \tau_y)$ (A2). As noted, this factor map points in the domain outside the TWs to the TW perimeter [see Fig. 7(a)] in such a way that more distant contours correspond to points further away from the touching point. In fact, since the field varies more slowly in these regions compared to the regions closer to the touching point, it is easier to calculate the scattered power rather than the absorbed power (which requires an integration over the rapidly varying near fields). Peculiarly, this magnetic-field-based calculation somehow transcends the quasistatic limit, thus providing a nonzero prediction for the scattered power.

Thus, we now proceed past the near-field calculation of [26] and compute analytically and numerically the SH scattered power from the TWs, $P_{\text{scat}}^{2\omega}$, given by

$$P_{\text{scat}}^{2\omega} = \frac{1}{2}\text{Re}\int_{\mathcal{S}} E_\phi^{2\omega}\left[H_z^{2\omega}\right]^* d\mathcal{S}. \tag{B1}$$

This is the scattered power that passes through the surface $\mathcal{S}$, where $\hat{n}$ represents the normal to the surface [see Fig. 7(a)].

To calculate the SH magnetic field (A1), we have to evaluate $J_{r,z}(\tau_x, \tau_y)$ (A2); this requires computing the analytic expression for the parallel derivative of the FF electric field $E_\perp^\omega(\tau_x, \tau_y)$. It is given by

$$\partial_\parallel[E_\perp^\omega(\tau_x, \tau_y)] = \mathcal{M} + \mathcal{N}, \tag{B2}$$

where

$$\mathcal{M} = \frac{iy\pi\alpha^\omega aE_{0x}^\omega}{\varepsilon_m^\omega + 1}\left[\frac{-i2ay^2 - i(x - a)^2(2x - \alpha^\omega a) + \frac{1}{2}a|y|\left[4a - \frac{6y^2}{a} - 2\alpha^\omega a\left(\frac{x-a}{a}\right)\right] + |y|^3}{|y|(x + i|y|)^4}\right]\exp\left(\frac{-\alpha^\omega a}{x + i|y|}\right), \tag{B3}$$

and

$$\mathcal{N} = \frac{-\text{sgn}[y]\pi\alpha^\omega aE_{0x}^\omega}{\varepsilon_m^\omega + 1}\left[\frac{(x - a)}{(x + i|y|)^2} - \frac{y[|y| - i(x - a)](i2|y| + 2x - \alpha^\omega a)}{(x + i|y|)^4}\right]\exp\left(\frac{-\alpha^\omega a}{x + i|y|}\right),$$

where E_{0x}^ω is the amplitude of the incident plane wave along the x direction. For all plots presented in this paper, we set it to unity. Now that we have all the expressions needed for the evaluation of the magnetic field (A1), we can analytically
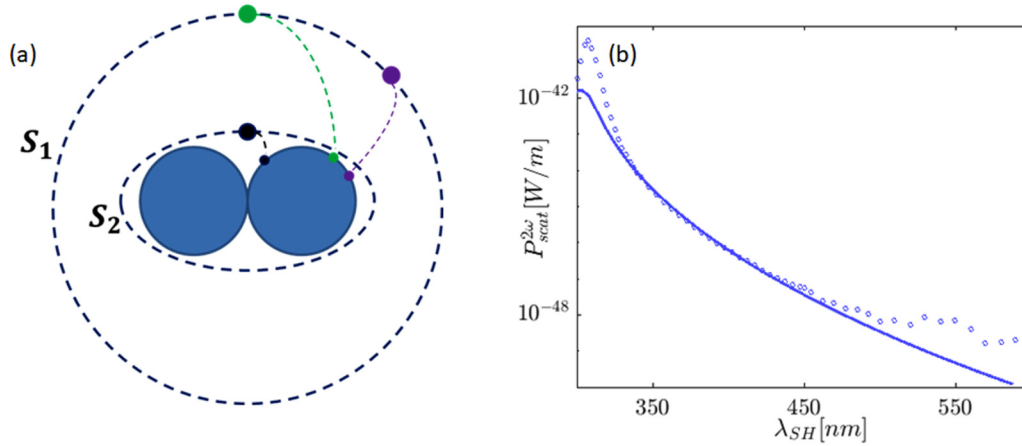
FIG. 7. (a) Two surfaces $\mathcal{S}_1$ and $\mathcal{S}_2$ surrounding the TWs. τ_x and τ_y map each point on these surfaces to the TW perimeter. For $\mathcal{S}_1$, with a radius of 22 nm, each point maps to points relatively far from the touching point. Conversely, for $\mathcal{S}_2$ which is closer to the TW structure, each point maps closer to the touching point. (b) The numeric (dots) and the analytic (blue solid line) solutions for the SH scattered power of TWs for $\varepsilon_{bg} = 1$.

calculate the SH parallel electric field, using

$$E_\phi^{2\omega}(r) = \frac{i}{2\omega\varepsilon_0\varepsilon_m^{2\omega}} \frac{\partial H_z^{2\omega}}{\partial r} \qquad (B4)$$

from the analytic expression for the magnetic field (A1). Here, $r = \sqrt{x^2 + y^2}$ is the radial coordinate along which the differentiation is performed.

In order to validate the solution described above, we support our analytic results by direct numeric simulations using COMSOL MULTIPHYSICS (v 3.5a) (see Appendix E in [26]). In fact, the numeric calculation of the derivatives in Eq. (B4)

required even higher resolution compared to the calculations in [26].

We observe good agreement between the analytic and numeric calculations for most of the spectral regime studied, with the exception of the lower frequency range (see Fig. 7). As we saw before [Eq. (5)], the fields peak closer to the touching point when material losses are lower, and are also more concentrated at lower frequencies [see Fig. 5(a)]. Thus, capturing this effect in numerical simulations is naturally harder. Indeed, the numeric results for the Drude loss parameter $\gamma = 0.2$ deviate from the analytic solution in the long-wavelength regime; better agreement was obtained in this regime for higher absorption (not shown).

[1] A. Bouhelier, M. Beversluis, A. Hartschuh, and L. Novotny, Near-Field Second-Harmonic Generation Induced by Local Field Enhancement, Phys. Rev. Lett. **90**, 013903 (2003).

[2] J. Mäkitalo, S. Suuriniemi, and M. Kauranen, Boundary element method for surface nonlinear optics of nanoparticles, Opt. Express **19**, 23386 (2011).

[3] N. Bloembergen, R. Chang, S. Jha, and C. Lee, Optical second-harmonic generation in reflection from media with inversion symmetry, Phys. Rev. **174**, 813 (1968).

[4] M. Scalora, M. Vincenti, D. de Ceglia, V. Roppo, M. Centini, N. Akozbek, and M. Bloemer, Second- and third-harmonic generation in metal-based structures, Phys. Rev. A **82**, 043828 (2010).

[5] G. Bachelier, J. Butet, I. Russier-Antoine, C. Jonin, E. Benichou, and P.-F. Brevet, Origin of optical second-harmonic generation in spherical gold nanoparticles: Local surface and nonlocal bulk contributions, Phys. Rev. B **82**, 235403 (2010).

[6] C. Ciracì, E. Poutrina, M. Scalora, and D. R. Smith, Origin of second-harmonic generation enhancement in optical split-ring resonators, Phys. Rev. B **85**, 201403(R) (2012).

[7] C. Ciracì, E. Poutrina, M. Scalora, and D. R. Smith, Second-harmonic generation in metallic nanoparticles: Clarification of the role of the surface, Phys. Rev. B **86**, 115451 (2012).

[8] K. Yoo, S. F. Becker, M. Silies, S. Yu, C. Lienau, and N. Park, Bridging microscopic nonlinear polarizations toward far-field second harmonic radiation, arXiv:1711.09568.

[9] S. Levi, R. Samueli, M. Choudhary, and A. Niv, Second-harmonic generation of electrostatic origin from extreme nanosized bi-metal structures, Opt. Lett. **43**, 3662 (2018).

[10] M. H. Shor, E. Toledo, S. Shital, A. Maity, Y. Sivan, M. Schvartzman, and A. Niv, Second-harmonic generation from subwavelength metal heterodimers, Opt. Express **28**, 31468 (2020).

[11] S. Roke, M. Bonn, and A. Petukhov, Nonlinear optical scattering: The concept of effective susceptibility, Phys. Rev. B **70**, 115106 (2004).

[12] G. Bachelier, I. Russier-Antoine, E. Benichou, C. Jonin, and P.-F. Brevet, Multipolar second-harmonic generation in noble metal nanoparticles, J. Opt. Soc. Am. B **25**, 955 (2008).

[13] J. Butet, J. Duboisset, G. Bachelier, I. Russier-Antoine, E. Benichou, C. Jonin, and P.-F. Brevet, Optical second harmonic generation of single metallic nanoparticles embedded in a homogeneous medium, Nano Lett. **10**, 1717 (2010).

[14] J. Butet, I. Russier-Antoine, C. Jonin, N. Lascoux, E. Benichou, and P.-F. Brevet, Nonlinear Mie theory for the second harmonic

generation in metallic nanoshells, J. Opt. Soc. Am. B **29**, 2213 (2012).

[15] J. Butet, S. Dutta-Gupta, and O. J. F. Martin, Surface second-harmonic generation from coupled spherical plasmonic nanoparticles: Eigenmode analysis and symmetry properties, Phys. Rev. B **89**, 245449 (2014).

[16] P. Ginzburg, A. Krasavin, Y. Sonnefraud, A. Murphy, R. Pollard, S. A. Maier, and A. Zayats, Nonlinearly coupled localized plasmon resonances: Resonant second-harmonic generation, Phys. Rev. B **86**, 085422 (2012).

[17] C. Garrett and F. Robinson, Miller's phenomenological rule for computing nonlinear susceptibilities, IEEE J. Quantum Electron. **2**, 328 (1966).

[18] M. Hentschel, T. Utikal, H. Giessen, and M. Lippitz, Quantitative modeling of the third harmonic emission spectrum of plasmonic nanoantennas, Nano Lett. **12**, 3778 (2012).

[19] K. O'Brien, H. Suchowski, J. Rho, A. Salandrino, B. Kante, X. Yin, and X. Zhang, Predicting nonlinear properties of metamaterials from the linear response, Nat. Mater. **14**, 379 (2015).

[20] I. Russier-Antoine, J. Duboisset, G. B. E. Benichou, C. Jonin, N. D. Fatti, F. Vallée, A. Sánchez-Iglesias, I. Pastoriza-Santos, L. Liz-Marzan, and P. F. Brevet, Symmetry cancellations in the quadratic hyperpolarizability of non-centrosymmetric gold decahedra, J. Phys. Chem. Lett. **1**, 874 (2010).

[21] J. Zyss and I. Ledoux, Nonlinear optics in multipolar media: Theory and experiments, Chem. Rev. **94**, 77 (1994).

[22] A. Salomon, M. Zielinski, R. Kolkowski, J. Zyss, and Y. Prior, Size and shape resonances in second harmonic generation from silver nanocavities, J. Phys. Chem. C **117**, 22377 (2013).

[23] C.-Y. Wang, H.-Y. Chen, L. Sun, W.-L. Chen, Y.-M. Chang, H. Ahn, X. Li, and S. Gwo, Giant colloidal silver crystals for low-loss linear and nonlinear plasmonics, Nat. Commun. **6**, 7734 (2015).

[24] M. Celebrano, X. Wu, M. Baselli, S. Grossmann, P. Biagioni, A. Locatelli, C. D. Angelis, G. Cerullo, R. Osellame, B. Hecht, L. Duo, F. Ciccacci, and M. Finazzi, Mode matching in multiresonant plasmonic nanoantennas for enhanced second harmonic generation, Nat. Nanotechnol. **10**, 412 (2015).

[25] S. Keren-Zur, L. Michaeli, H. Suchowski, and T. Ellenbogen, Shaping light with nonlinear metasurfaces, Adv. Opt. Photonics **10**, 309 (2018).

[26] K. N. Reddy, P. Y. Chen, A. I. Fernández-Domínguez, and Y. Sivan, Surface second-harmonic from metallic nanoparticle configurations—A transformation optics approach, Phys. Rev. B **99**, 235429 (2019).

[27] J. B. Pendry, D. Schurig, and D. R. Smith, Controlling electromagnetic fields, Science **312**, 1780 (2006).

[28] J. B. Pendry, A. Aubry, D. R. Smith, and S. A. Maier, Transformation optics and subwavelength control of light, Science **337**, 549 (2012).

[29] P. Huidobro, M. Nesterov, L. Martin-Moreno, and F. Garcia-Vidal, Transformation optics for plasmonics, Nano Lett. **10**, 1985 (2010).

[30] Y. Luo, R. Zhao, A. I. Fernández-Domínguez, S. A. Maier, and J. B. Pendry, Harvesting light with transformation optics, Sci. China Inf. Sci. **56**, 1 (2013).

[31] P. A. Huidobro and A. I. Fernández-Domínguez, Transformation optics for plasmonics: From metasurfaces to excitonic strong coupling, C. R. Phys. **21**, 389 (2020).

[32] A. Aubry, D. Lei, A. I. Fernández-Domínguez, Y. Sonnefraud, S. A. Maier, and J. B. Pendry, Plasmonic light-harvesting devices over the whole visible spectrum, Nano Lett. **10**, 2574 (2010).

[33] D. Y. Lei, A. Aubry, S. A. Maier, and J. B. Pendry, Broadband nano-focusing of light using kissing nanowires, New J. Phys. **12**, 093030 (2010).

[34] K. N. Reddy, P. Y. Chen, A. I. Fernández-Domínguez, and Y. Sivan, Revisiting the boundary conditions for second-harmonic generation at metal-dielectric interfaces, J. Opt. Soc. Am. B **34**, 1824 (2017).

[35] Note that as in [26], we chose a relatively high value for the imaginary part of the metal permittivity, corresponding to low quality metal nanostructures. This choice is appropriate for several fabrication techniques and accounts for quantum size effects and nonlocality [77]; this choice also ensured convergence of the numerical simulations.

[36] Thus, providing additional motivation to focus on that regime only.

[37] A. Boardman, *Electromagnetic surface modes* (Wiley, New York, 1982).

[38] C. I. Valencia, E. R. Méndez, and B. S. Mendoza, Second-harmonic generation in the scattering of light by two-dimensional particles, J. Opt. Soc. Am. B **20**, 2150 (2003).

[39] Note that the underlying rapid oscillations [26] can be seen only via the real part of the field (see also Fig. 5).

[40] Peculiarly, since previous studies of this problem focused on a comparison of the spectral bandwidth of these two structures, this result was not noted previously.

[41] L. R.-Q, F. J. García-Vidal, and A. I. Fernández-Domínguez, Plasmon-exciton coupling in symmetry-broken nanocavities, ACS Photonics **5**, 177 (2018).

[42] Ideally, one desires to have the optimal parameters such that $1/|\mathcal{P}|$ diverges; in this case, the geometric factor x will have little consequence. However, as we consider a lossy metal, $1/|\mathcal{P}|$ attains its maximum value instead of diverging.

[43] Similarly, higher losses tend to pull the peak position of $E_\perp^\omega$ away from the touching point; this is indeed intuitive—the absorption limits the near-field enhancement [32].

[44] A. I. Fernández-Domínguez, P. Zhang, Y. Luo, S. A. Maier, F. J. Garcia-Vidal, and J. B. Pendry, Transformation-optics insight into nonlocal effects in separated nanowires, Phys. Rev. B **86**, 241110(R) (2012).

[45] H. Suchowski, G. Porat, and A. Arie, Adiabatic processes in frequency conversion, Laser Phys. Rev. **8**, 333 (2014).

[46] O. Yaakobi and L. Friedland, Autoresonant 4-wave mixing in optical fibers, Phys. Rev. A **82**, 023820 (2010).

[47] It is worth noting that the additional factor $\sim \omega \sinh 2\alpha^\omega / \alpha^\omega$ also contributes to the spectral narrowing.

[48] L. Novotny and B. Hecht, *Principles of nano-optics* (Cambridge University Press, Cambridge, UK, 2006).

[49] P. Y. Chen, D. J. Bergman, and Y. Sivan, Generalizing Normal Mode Expansion of Electromagnetic Green's Tensor to Lossy Resonators in Open Systems, Phys. Rev. Appl. **11**, 044018 (2019).

[50] T.-Y. Chen, J. Obermeier, T. Schumacher, F.-C. Lin, J.-S. Huang, M. Lippitz, and C.-B. Huang, Modal symmetry controlled second-harmonic generation by propagating plasmons, Nano Lett. **19**, 6424 (2019).

[51] A. I. Fernández-Domínguez, A. Wiener, F. J. Garcia-Vidal, S. A. Maier, and J. B. Pendry, Transformation-Optics Description of Nonlocal Effects in Plasmonic Nanostructures, Phys. Rev. Lett. **108**, 106802 (2012).

[52] Those occur for the Ag used here on wavelengths shorter than ≈ 350 nm; they were intentionally neglected in order to allow focusing on the wave aspects of the problem. These effects would naturally increase the absorption and limit the near-field enhancement and the scattering.

[53] M. A. Vincenti, D. de Ceglia, V. Roppo, and M. Scalora, Harmonic generation in metallic, GaAs-filled nanocavities in the enhanced transmission regime at visible and UV wavelengths, Opt. Express **19**, 2067 (2011).

[54] M. Scalora, M. Vincenti, D. de Ceglia, N. Akozbek, V. Roppo, M. Bloemer, and J. Haus, Dynamical model of harmonic generation in centrosymmetric semiconductors at visible and UV wavelengths, Phys. Rev. A **85**, 053809 (2012).

[55] D. Rocco, V. F. Gili, L. Ghirardini, L. Carletti, V. Favero, A. Locatelli, G. Marino, D. N. Neshev, M. Celebrano, M. Finazzi, G. Leo, and C. D. Angelis, Tuning the second-harmonic generation in AlGaAs nanodimers via non-radiative state optimization, Photonics Res. **6**, B6 (2018).

[56] L. Carletti, C. Li, J. Sautter, I. Staude, C. D. Angelis, T. Li, and D. N. Neshev, Second harmonic generation in monolithic lithium niobate metasurfaces, Photonics Res. **27**, 33391 (2019).

[57] M. F. Picardi, M. Neugebauer, J. Eismann, G. Leuchs, P. Banzer, F. J. R. Fortuno, and A. V. Zayats, Experimental demonstration of linear and spinning Janus dipoles for polarization- and wavelength-selective near-field coupling, Light: Sci. Appl. **8**, 52 (2019).

[58] A. Aubry, D. Lei, S. A. Maier, and J. B. Pendry, Broadband plasmonic device concentrating the energy at the nanoscale: The crescent-shaped cylinder, Phys. Rev. B **82**, 125430 (2010).

[59] A. Aubry, D. Lei, S. A. Maier, and J. B. Pendry, Plasmonic hybridization between nanowires and a metallic surface: A transformation optics approach, ACS Nano **5**, 3293 (2011).

[60] Y. Luo, D. Y. Lei, S. A. Maier, and J. B. Pendry, Broadband Light Harvesting Nanostructures Robust to Edge Bluntness, Phys. Rev. Lett. **108**, 023901 (2012).

[61] F. Yang, E. Galiffi, P. A. Huidobro, and J. B. Pendry, Nonlocal effects in plasmonic metasurfaces with almost touching surfaces, Phys. Rev. B **101**, 075434 (2020).

[62] F. Yang, P. A. Huidobro, and J. B. Pendry, Transformation optics approach to singular metasurfaces, Phys. Rev. B **98**, 125409 (2018).

[63] A. I. Fernández-Domínguez, S. A. Maier, and J. B. Pendry, Collection and Concentration of Light by Touching Spheres: A Transformation Optics Approach, Phys. Rev. Lett. **105**, 266807 (2010).

[64] Y. Luo, R. Zhao, and J. Pendry, van der Waals interactions at the nanoscale: The effects of nonlocality, Proc. Natl. Acad. Sci. U.S.A. **111**, 18422 (2014).

[65] Z. Ruan, G. Veronis, K. Vodopyanov, M. Fejer, and S. Fan, Enhancement of optics-to-THz conversion efficiency by metallic slot waveguides, Opt. Express **17**, 13502 (2009).

[66] F. Che, S. A. Ponomarenko, and M. Cad, Giant spectral transformations in plasmon-enhanced difference-frequency generation with polychromatic light, J. Opt. **18**, 125503 (2016).

[67] B. Metzger, M. Hentschel, M. Nesterov, T. Schumacher, M. Lippitz, and H. Giessen, Nonlinear optics of complex plasmonic structures: Linear and third-order optical response of orthogonally coupled metallic nanoantennas, Appl. Phys. B **122**, 77 (2016).

[68] E. Minerbi, S. Keren-Zur, and T. Ellenbogen, Nonlinear metasurface Fresnel zone plates for terahertz generation and manipulation, Nano Lett. **19**, 6072 (2019).

[69] M. P. Nielsen, X. Shi, P. Dichtl, S. A. Maier, and R. F. Oulton, Giant nonlinear response at a plasmonic nanofocus drives efficient four-wave mixing, Science **358**, 1179 (2017).

[70] S. Hanham, A. I. Fernández-Domínguez, J. H. Teng, S. S. Ang, K. P. Lim, S. F. Yoon, C. Y. Ngo, N. Klein, J. B. Pendry, and S. A. Maier, Broadband terahertz plasmonic response of touching InSb disks, Adv. Mater. **24**, OP226 (2012).

[71] D. Lei, A. I. Fernández-Domínguez, Y. Sonnefraud, K. Appavoo, R. F. Haglund, J. B. Pendry, and S. A. Maier, Revealing plasmonic gap modes in particle-on-film systems using dark-field spectroscopy, ACS Nano **6**, 1380 (2012).

[72] Note that this is far simpler than transforming each of the constituents of the polarization source—the $\chi^{(2)}$ tensor, and each of the FF fields.

[73] This approach proved to be simpler than the WKB approximation employed in [44,51] for the linear nonlocal response.

[74] $\alpha^\omega = |k| d$ where k is the spatial Fourier transform coordinate; in the quasistatic limit, it represents the propagation constant as well as the mode transverse width.

[75] As explained in [26], $\mathcal{P}$ differs from the potentially more familiar PM factor; see, e.g., [78] (which is sinc$[(\alpha^{2\omega} - 2\alpha^\omega)d]$); they vanish together, but $\mathcal{P}$ is more informative as it includes information about the profile of additional modes (of the same symmetry).

[76] A. Aubry, D. Lei, S. A. Maier, and J. B. Pendry, Conformal transformation applied to plasmonics beyond the quasistatic limit, Phys. Rev. B **82**, 205109 (2010).

[77] N. A. Mortensen, S. Raza, M. Wubs, T. Sondergaard, and S. I. Bozhevolnyi, A generalized non-local optical response theory for plasmonic nanostructures, Nat. Commun. **5**, 3809 (2014).

[78] R. W. Boyd, *Nonlinear optics*, 2nd ed. (Academic, New York, 2003).